Thermal shock and residual strength testing of SiC/SiC composite braided tubes

Q. Xu[1] · X. Jin[1,*] · L. Liu[1] · C. Hou[1] · N. Hu[1] · J. Chen[1] · S. Zhao[2] · T. J. Marrow[2] · X. Fan[1,*]

[1] *Joint Research Center for Extreme Environment and Protection Technology, State Key Laboratory for Strength and Vibration of Mechanical Structures, School of Aerospace Engineering, Xi'an Jiaotong University, Xi'an, 710049, China.*

[2] *Department of Materials, Oxford University, Parks Rd, Oxford, OX1 3PH, UK.*

Abstract

Background Ceramic matrix composites are promising materials for high temperature application in aerospace and nuclear engineering. In these applications, thermal shock is an important potential cause for failure. **Objective** In order to study thermal shock resistance of SiC/SiC composite braided tubes, a novel method has been developed to apply thermal shock cycles to tube sections and then measure the residual tensile strength. **Methods** SiC/SiC composite braided tubes have been thermally shocked by many cycles in a short time using a novel test platform based on quartz lamp irradiation heating. The circumferential tensile strength was measured using C-ring specimens after thermal shock testing of short tube sections. Numerical simulations of the stress from the thermal shock test were conducted using the finite element method. **Results** The circumferential tensile strength decreased with increasing number of thermal shock cycles in air. An embrittled region with limited fiber pullout due to oxidation extended from the surface. **Conclusions** The test platform can simulate service environments with fast temperature cycling for small test specimens in air.

Keywords: Ceramic matrix composites · SiC/SiC · thermal shock resistance · tensile strength · oxidation

1. Introduction

The demanding fields of aerospace and nuclear energy have set significant requirements for the high-temperature mechanical properties of materials [1-2]. For

* Corresponding authors.
E-mail address: jinxiaochao@xjtu.edu.cn (X.C. Jin); fanxueling@mail.xjtu.edu.cn (X.L. Fan).

example, the combustion chamber outlet temperature of the fourth-generation aero-engines has reached 1700 ℃, while the existing superalloys have a physical temperature limit of 1100 ℃ [3]. In thermally efficient advanced nuclear systems, such as gas-cooled fast reactors, lead-cooled fast reactors and very-high-temperature reactors, the potential cladding materials will experience temperatures over 850°C in normal operation; the limit temperature of the zirconium alloys commonly used in light water reactors is around 400 °C, and these cannot meet the temperature requirements for fuel cladding [4].

Due to their high specific strength, good thermal stability and good oxidation resistance, woven ceramic matrix composites (CMCs) such as SiC/SiC CMCs are one of candidate material for extreme temperatures. In the aerospace and nuclear industries, woven CMCs have been recommended as materials for combustion chambers, turbine blades, nuclear fuel cladding and other key components [5-9]. However, during start-stop and transient maneuvers, the temperature of these components changes abruptly, which may result in severe thermal stresses and cause thermomechanical damage in the components. Compared to metals, CMCs possess a lower thermal conductivity combined with lower fracture toughness and can fail under such transient thermal conditions. Investigation of the cyclic thermal shock behavior of the CMCs have become important for the application of these materials [8,10].

Few studies on the thermal shock behavior of CMCs have been reported. Yang et al. [11] experimentally studied microstructural evolution in oxide/oxide CMCs under thermal shock, and introduced a thermal shock damage model to describe monotonic and cyclic thermal shock damage processes. Tong et al. [12] evaluated the thermal shock resistance of continuous carbon fiber reinforced ZrC-based ultra-high temperature CMCs (C/C-ZrC). The residual strength and mass variation of the as-prepared composite under different thermal shock cycles and temperatures were tested to characterize the thermal shock resistance. Yang et al. [13] established thermo-mechanical loading conditions-structure-property linkages for thermal aged oxide/oxide CMCs under cyclic thermal shocks, and constructed a correlation between porosity and strain energy release rate. Wang et al. [14] studied the thermal shock

behavior of three types of continuous fiber-reinforced CMCs using water quenching and showed that matrix cracking and delamination were the main mechanisms of thermal shock damage. However, these studies were only carried out over a small number of thermal shock cycles, and the degradation of mechanical properties of CMCs after hundreds and thousands of thermal shock cycles has not been studied. A major reason for this is the lack of a rapid heating technology for thermal shock.

For thermal shock testing of engineering materials, electromagnetic heating and resistance heating are commonly used. Electromagnetic heating has the advantages of non-contact, fast heating speed, and local heating [15], as well as the disadvantages of skin effect [16], large thermal inertia, and inability to heat non-metallic materials. Resistance heating has the advantages of simple and reliable structure, low cost and high power, as well as the disadvantages of large thermal inertia [17]. It also requires a sufficiently electrically conductive material. In recent years, due to its advantages of rapid heating and small thermal inertia, quartz lamp irradiation has attracted interest [18]. It is suitable for multiple thermal shock cycles tests but there are no reports on its application to CMCs. Due to lack of a rapid heating technology, the pseudoplastic fracture mechanism and strength degradation relationship of CMCs caused by hundreds and thousands of thermal shock cycles is not yet clear.

Therefore, to study the thermal shock resistance and failure mechanisms of CMCs, a thermal shock test platform based on quartz lamp irradiation heating has been developed. Using the platform, thermal shock tests for SiC/SiC composite braided tubes (hereinafter referred to as braided tubes) have been carried out. The strength degradation caused by cyclic thermal shock has been measured using C-ring specimens, extracted from the tubes after thermal shock testing. Simple modelling of the stress developed in a thermal shock cycle provided insight into the initiation of cracking in the microstructure, and scanning electron microscopy (SEM) has been used to investigate the damage propagation mechanism.

2. Materials and Methods

2.1 Materials

The samples of braided tubes, as shown in Fig. 1(a), were obtained via the MatISSe EU FP7 project [19] and had been fabricated [20] by the CEA (French Alternative Energies and Atomic Energy Commission) [21]. They were made of third generation HNS SiC fibers (Hi-Nicalon™ Type-S, Nippon Carbon Co.) with an average diameter of 12 μm. As illustrated in Fig. 1(b), the fiber architecture consisted of three layers. The inner layer was a filament winding layer with a ±45° stacking configuration. The intermediate and outer layers were both 2×2 (±45°) two-dimensional braided structure. The fabric preform had been deposited with a 100 nm pyrolytic carbon (PyC) and then densified with a monolithic SiC matrix by the Chemical Vapor Infiltration (CVI) process. The braided tube specimens had a smooth ground inner surface with a radius of 3.90 mm. The external surface had roughness due to the as-woven structure, as presented in Fig. 1(c), with an outer radius of 4.88 mm. The mechanical properties of braided tubes in the elastic regime were measured by Zhao et al. [21] and summarized in Table 1.

Table 1: the elastic properties of the SiC/SiC composite at room temperature and 900°C.

Temperature/℃	Elastic modulus/GPa	Proportional limit stress/MPa
25	335±25	247±15
900	327±21	170±12

2.2. Thermal shock test platform

The thermal shock test platform, which is based on the quartz lamp irradiation heating technique, consists of a master computer, a programmable logic controller (PLC) module, power controller, air cooling pump, heating module and so on (Fig. 2(a)). The master computer gives instructions to the PLC module, which provides data to the master computer. The PLC module sends control signals to the power controller, which controls the output power of the heating module to heat the specimen. At the same time, the temperature signals of the specimen are collected by temperature sensor (i.e., the

K-type thermocouple) and standard signals are transmitted to the PLC module through the temperature acquisition module. The power controller and the PLC module are supplied by high power. In addition, water and air are used to cool the clamps of the quartz lamp array and specimens. The test platform control mode is presented in Fig. 2(b).

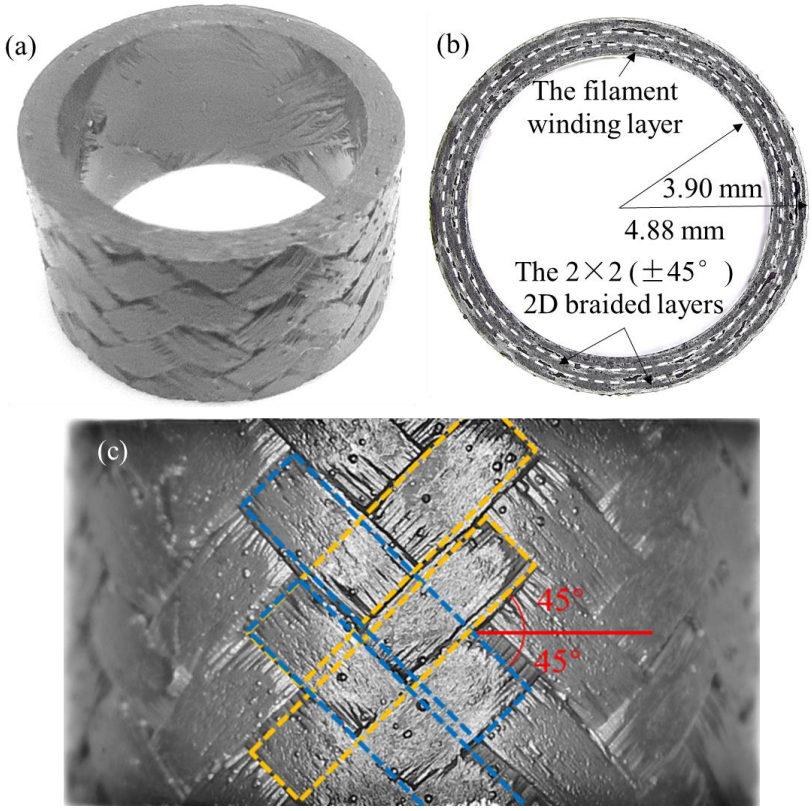

Fig. 1 Optical images of a SiC/SiC composite braided tube specimen (axial length 5 mm, diameter ~10 mm): (a) macroscopic morphology; (b) cross-section to show the three layers of the tube and dimensions; (c) the 2×2 2D braided structure at the outer surface

As shown in Fig. 3, the heating module includes four main parts: the quartz lamp array, clamp, cooling channel and K-type thermocouple. The cooling water and air channels are embedded in the clamp and the quartz lamp array. During the thermal cycle test, the specimen was fixed in a mullite plate by high-temperature resistant alloy wire, in direct contact with the thermocouple tip and heated by the quartz lamp array. In the cooling process, the specimen was cooled by a water spray.

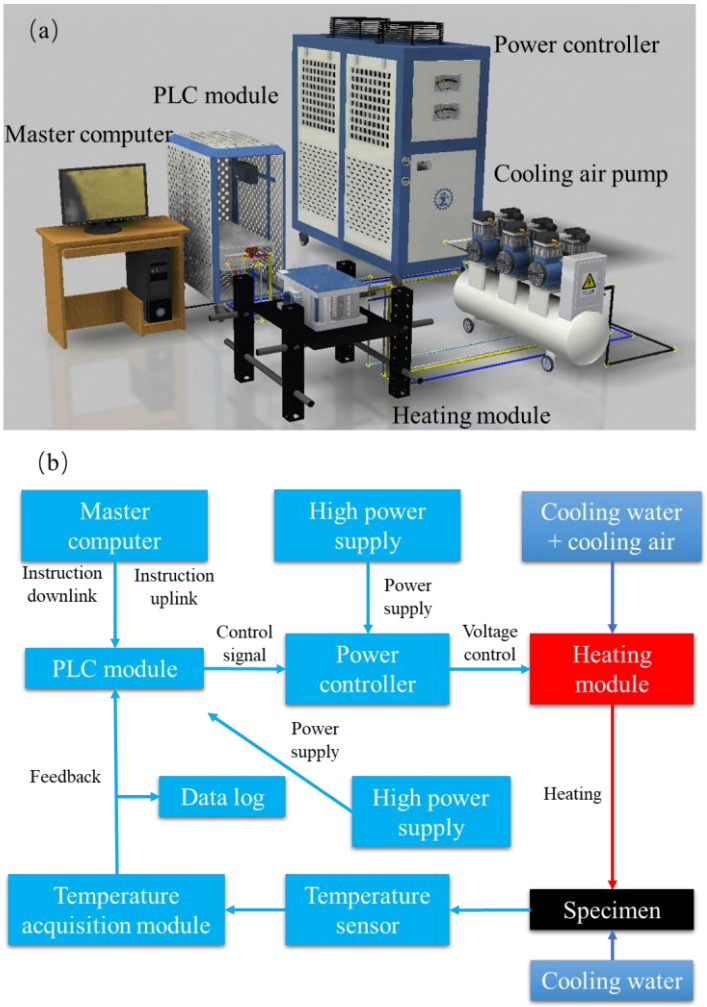

Fig. 2 Thermal shock test platform: (a) platform components; (b) platform control mode

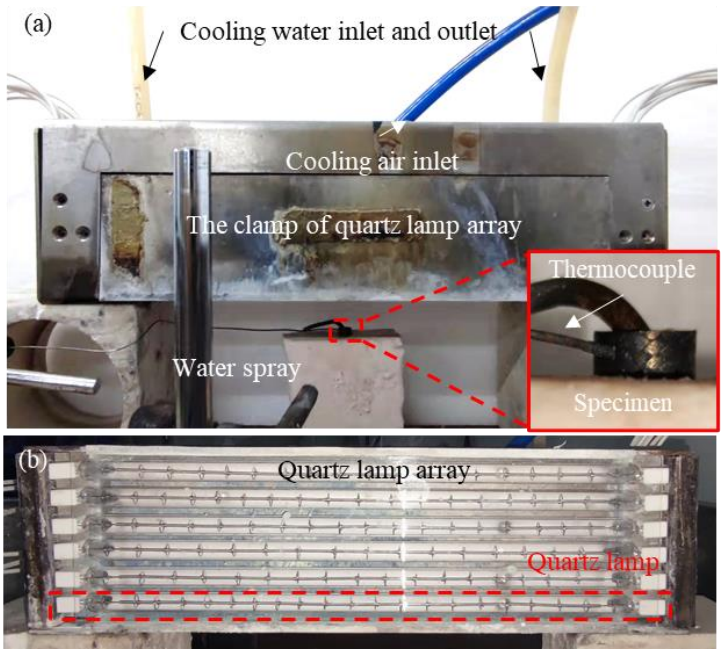

Fig. 3 The heating module: (a) front view; and (b) bottom view

2.3. Thermal Cycling: Experimental Method and Numerical Simulation

A total of 6 groups of 4 specimens each were subjected to 0, 250, 500, 750, 1000 and 1250 thermal shock cycles, respectively (i.e., 24 test samples were used in total). Each thermal shock cycle had a total duration of 110s, and comprising heating for 40s, high-temperature hold for 30s, cooling for 30s and low-temperature hold for 10s. The maximum and minimum objective temperatures were 1000℃ and 20℃ respectively. Example temperature curves for the thermal shock tests are illustrated in Fig. 4, showing that the maximum rates of heating and cooling of the platform could reach 40 °C·s^{-1} and 60 °C·s^{-1} respectively.

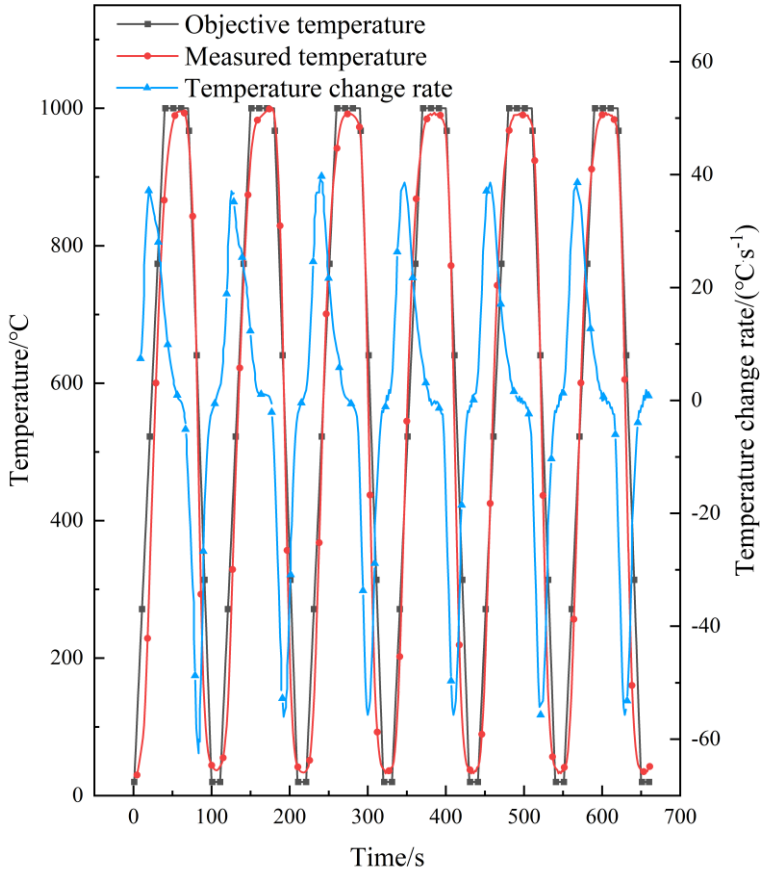

Fig. 4 Example data for the measured temperature and temperature change rate for thermal shock testing between objective temperatures of 1000°C and 20°C of a SiC/SiC composite tube specimen

The heat source was at a distance of 12 mm above the specimen along its axial direction. Numerical simulations of the thermal shock test were conducted using the finite element method, with the objective of estimating the maximum thermal stress in

the microstructure. The model, shown in Fig. 5, aimed for heating conditions similar to the experiment (Fig. 3). The upper surface of the fluid domain was the heat source. The braided tube, which has a wall thickness that is small (~10%) compared to its diameter, would absorb and radiate heat mainly through its outer and inner circumferential surfaces. In this condition the temperature gradient across the wall thickness became sufficiently small to be ignored, and thermal stresses rose mainly from the relative dimensional changes of the fiber bundles and matrix. To represent the test specimen, a simplified model of the outer layer of the braided tube was established in ANSYS according to the specimen manufacture, in which the fiber bundles were first braided to form a layered fiber bundle preform, followed by deposition of the interphase and matrix via the CVI process [22]. Regular braiding of the fiber bundles was represented, where each bundle crossed above and below two other bundles. The model was divided into two materials due to their differences in properties. One part ("fiber bundles") contained fiber bundles, and the other part ("matrix") didn't contain fibers, as illustrated in Fig. 5. Previous studies [23-26] showed that sufficiently accurate results could be obtained when the bundle cross-sections were constant. The shape of cross-sections of the fiber bundles and the matrix in this model were respectively defined using an ellipse (major diameter 700 μm, minor diameter 70 μm, eccentricity 0.995) and partially overlapping elliptical rings (major diameter 840 μm, minor diameter 150 μm, eccentricity 0.984). The volume fraction of fiber bundles with respect to the volume fraction of matrix was 0.73, and the length of the model was 3 mm. Their dimensions were obtained from measurements by SEM (see supplementary information). The internal porosity of the composite microstructure was neglected. The fluid in the domain was air, and gravity was considered in the simulation of natural convection. The Boussinesq hypothesis was adopted for the density of fluid, and the relationship between density and temperature was included in the buoyancy term. The initial density and thermal expansion coefficient were 1.184 $kg \cdot m^{-3}$ and 3400×10^{-6} K^{-1} respectively. The details of the numerical simulations are provided in the supplementary materials.

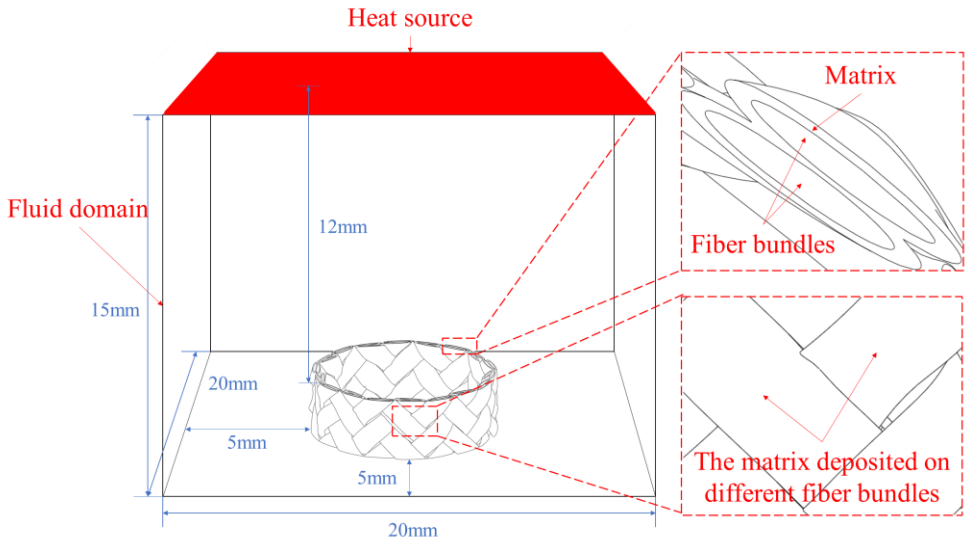

Fig. 5 Schematic of the numerical simulation of the thermal cycling

In the numerical simulations, it was assumed that the properties of the two constituent materials (fiber bundles and matrix) were temperature independent, linear elastic, and isotopic. The effects of high-temperature creep and oxidation were neglected [27]. The material parameters used are listed in Table 2. Further details of the numerical simulations, which found the predicted temperature change was consistent with the objective temperature in experiments, are given in Supplementary information.

Table 2: Material parameters of the fiber bundles and matrix in the numerical simulation of SiC/SiC composites braided tubes [21].

Material parameters	Fiber bundles	Matrix
Density /$kg{\cdot}m^{-3}$	3100	3220
Young's modulus /GPa	420	180
Poisson ratio	0.218	0.728
Thermal expansion coefficient /$10^{-6}\ K^{-1}$	5.1	4.6
Thermal conductivity /$W{\cdot}(m\ K)^{-1}$	18.4	20
Specific heat capacity/$J{\cdot}(kg℃)^{-1}$	700	530

2.4. C-Ring diametral compression test

The braided tube is a candidate nuclear material for fuel cladding, for which it is important to know the resistance to tensile hoop stress that may come from internal gas pressure or fuel expansion [28-29]. Mechanical tests were carried out to determine the

circumferential tensile strength of the braided tubes after different numbers of thermal shock cycles. In order to measure the hoop properties of tubular components for the purpose of materials qualification, simple specimens such as C-rings [30] and O-rings [31] have been proposed. In this work, based on the ASTM C1323−10 standard [32], C-ring specimens were tested.

After thermal shock testing, each braided tube was cut across its diameter into 2 C-rings using a diamond-coated wire with a diameter of about 0.35 mm. The cut surfaces were ground with 2000 grit SiC paper until no obvious defects were observed under the optical microscope. As shown in Fig. 6(a), a microcomputer controlled electronic universal testing machine (MTS, C45.105) was used for diametral compression testing with a loading rate of 0.1 mm/min. A 1.5 mm deep groove at the center of the loading anvils limited the movement of both ends of the C-shaped specimen during compression.

The ultimate circumferential (hoop) tensile strength was obtained from the critical failure force. According to curved beam theory (See Appendix) the maximum circumferential stress $\sigma_{\theta\max}$ is given by:

$$\sigma_{\theta\max} = \frac{6FR}{bh^2(1+\frac{h}{2R})} \tag{1}$$

where R is radius (at the mid-thickness of the tube wall), F is the force, h is the thickness of the tube wall, as illustrated in Fig. 6(b).

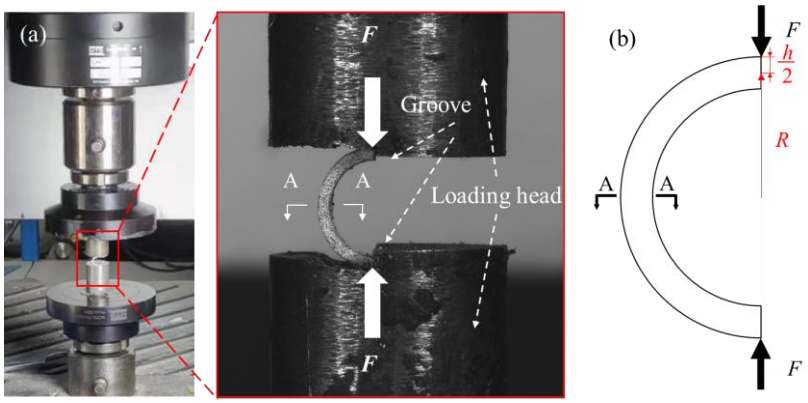

Fig. 6 Diametral compression test for C-ring specimens of SiC/SiC composite braided tube; (a) specimen set-up, (b) specimen dimensions, where R is radius at the mid-thickness of the tube wall, F is the force, and h is the thickness of the tube wall

3. Results and discussion

3.1. Mechanical behavior

Representative force-displacement curves from each group after 0, 250, 500, 750, 1000 and 1250 thermal shock cycles are presented in Fig. 7. The peak load, which defines the end of the nonlinear pre-fracture stage, decreased with increasing number of thermal shock cycles. The specimens showed a change in post-fracture behavior with increasing numbers of thermal shock cycles. Those with 0 and 250 cycles showed quite brittle fracture, while the specimens that received over 500 cycles showed pseudoplastic fracture. Moreover, with increasing numbers of thermal shock cycles, the pseudoplastic fracture behavior was more obvious.

The observed behavior is similar to previous studies of C-ring tests of the same material that had not been thermally shocked [21, 33], in which mechanical damage initiated first at the location of the maximum tensile stress in the outer layer of CVI-SiC matrix. Those studies observed that with increasing load, multiple matrix cracks occurred at the outer surface, and these cracks propagated into the fiber-rich regions of the specimen. The matrix crack density at the surface increased with load, and specimen fracture occurred after the peak load with propagation of a critical crack, typically at the mid-section (A-A).

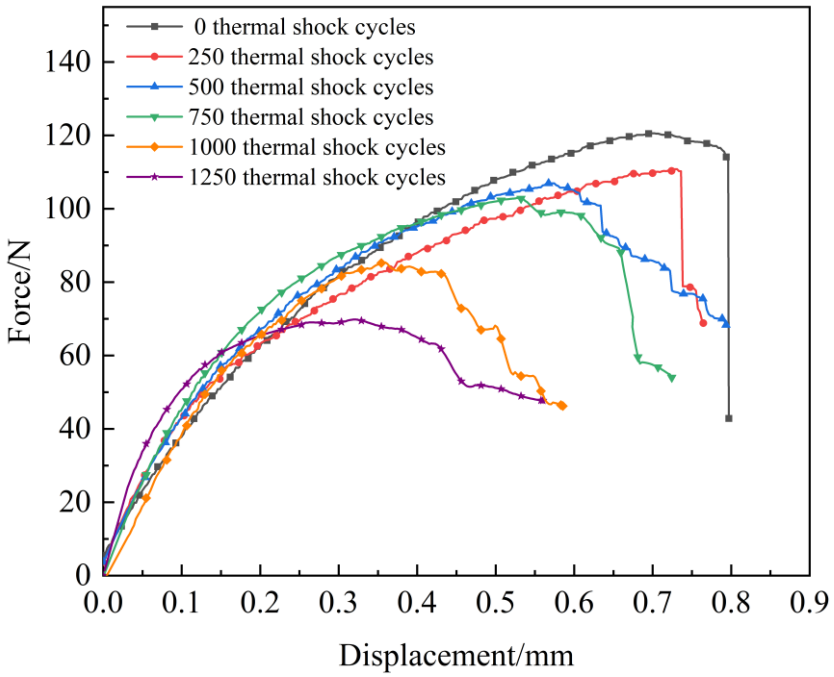

Fig. 7 Representative force-displacement curves after different numbers of thermal shock cycles

3.2. Strength degradation with number of cyclic thermal shocks

The mechanical test data are summarized in Fig 8, which shows that the ultimate circumferential tensile strength decreased with increasing number of thermal shock cycles (the numerical data are provided as supplementary material). Previous studies that determined the hoop strength of ceramic composite tubes from mechanical tests used an assumption of material uniformity [34]. The test specimens in this study have similar defect sizes and distribution, the same fiber architecture, and minimal density differences [21], and so are also regarded as uniform. A linear fit to the data gives an empirical formula of the strength degradation,

$$\sigma_{CTS} = \mathrm{a} + \mathrm{b}N \tag{2}$$

where σ_{CTS} is the circumferential tensile strength; N is the number of thermal shock cycles; a is the intercept (597.0±20.0 MPa); b is the gradient (-0.224±0.026). The correlation between circumferential tensile strength and number of thermal shock cycles is strong, with a Pearson' r coefficient of -0.876, and R-squared coefficient of 0.767.

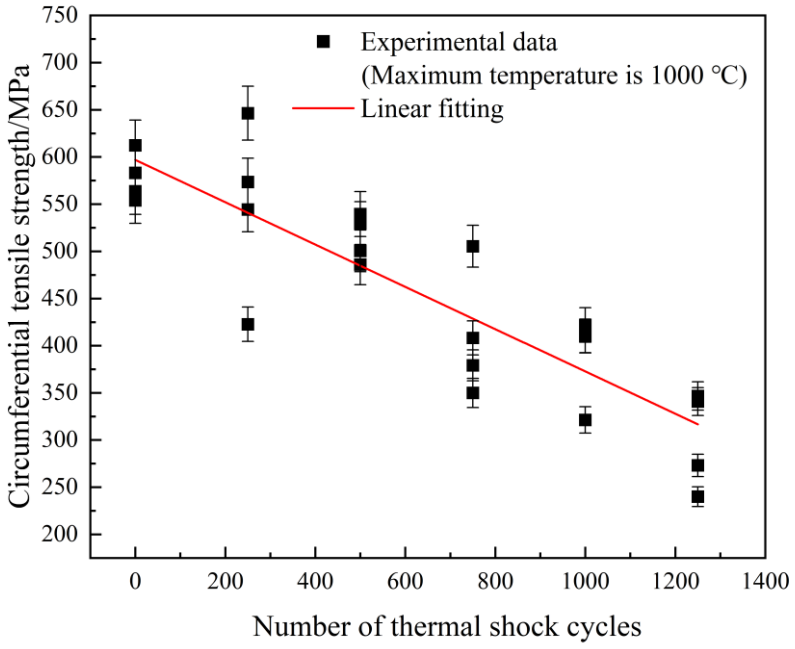

Fig. 8 The circumferential tensile strength (equation 1) after different numbers of thermal shock cycles, whose temperature range is 20°C-1000°C. The error bars represent the measurement uncertainty, derived from the load and dimensional precision (±0.5% and 0.03 mm respectively)

3.3. Damage evolution mechanism

Fig. 9a shows the predicted distribution of thermal stress at the outer surface of a specimen when the maximum temperature on surface rises to 1000°C (e.g., at a time of 40s in Fig. 4) in one thermal shock cycle, and its comparison in Fig. 9(b) with the surface of the material observed after 750 thermal shock cycles. The simulation predicts local tensile stress concentrations, which are coincident with changes in the surface geometry of the SiC matrix that is deposited on the fiber bundles. In the SEM image (Fig. 9(b) and Fig. 9(c)), the green and red areas are respectively the matrix deposited on the lower fiber bundles and the matrix deposited on the upper fiber bundles, and one such stress concentration is shown in the region in the red box of Fig. 9(a). The observed surface cracks converge at the predicted stress concentration. This behavior can be explained by considering the anisotropic nature of the CMC along with porosity, which generated local self-constraining surfaces with high thermal stress concentration that induced the formation of cracks [35].

Fig. 10 shows the predicted thermal stress distribution in a cross-section of the specimen when the maximum temperature on surface is 1000°C (e.g., at a time of 40s in Fig. 4) in one thermal shock cycle. It is compared with the fracture surfaces of specimen tested after 250 and 1250 thermal shock cycles. The thermal tensile stress, due to the differential thermal expansion of the fiber tows, is predicted to concentrate in the matrix between the two fiber bundles and to the side of fiber bundles, as illustrated in the dotted boxes in the Fig. 10(a). The SEM images of the fracture surface (for a specimen tested for 250 cycles) shows significant fiber pullout and also cracks between the two fiber bundles marked by dotted boxes in Fig. 10(b); the position of the cracks is similar to that of area II in Fig. 10(a). The SEM image shows that there are not only in-plane displacements (shear), but also out-of-plane displacements (opening) between the differently oriented fiber bundles. These are due to the complex pattern of

deformation that develops during the mechanical testing of the inhomogeneous composite material.

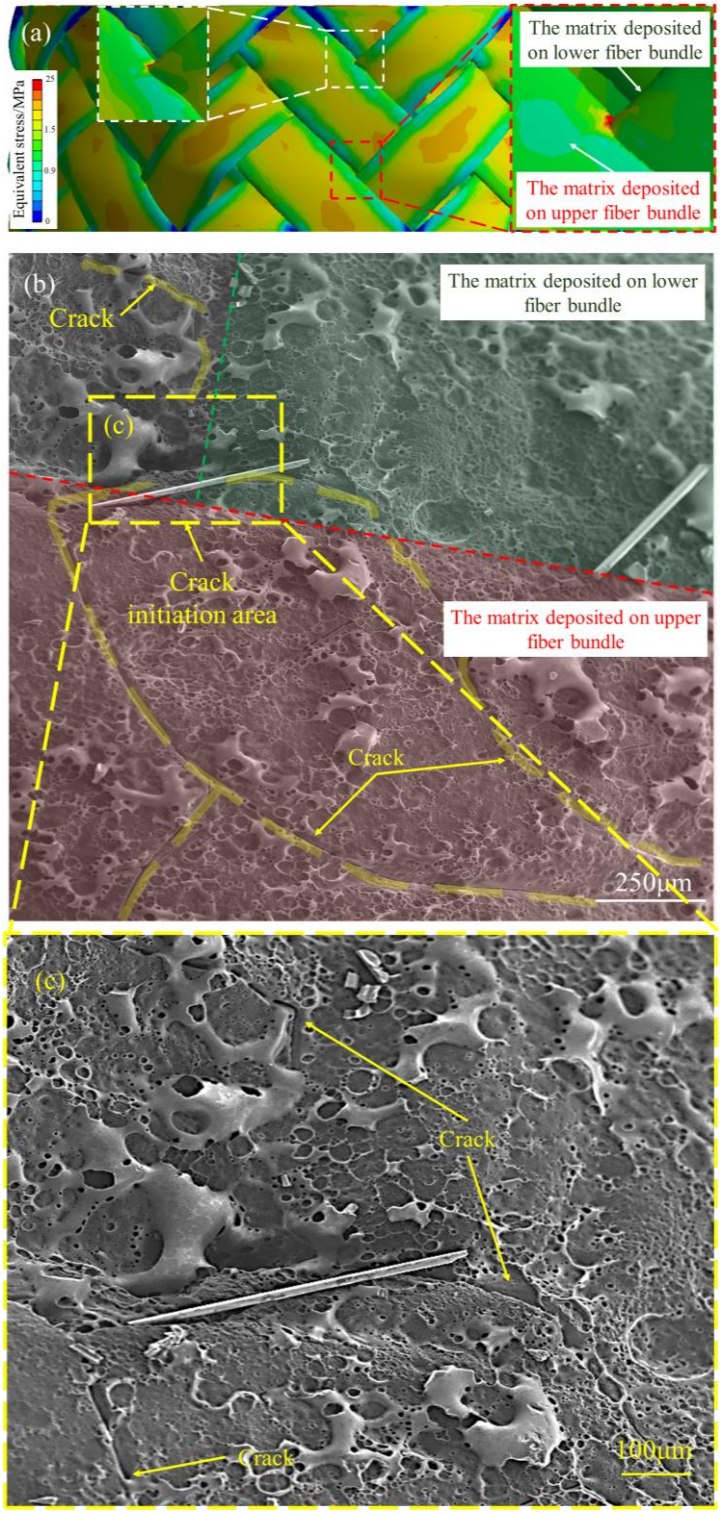

Fig. 9 The predicted surface stress distribution and surface morphology of the specimen: (a) predicted stress field due to heating from 20°C to 1000°C; (b) and (c) SEM image of a specimen

after 750 thermal shock cycles

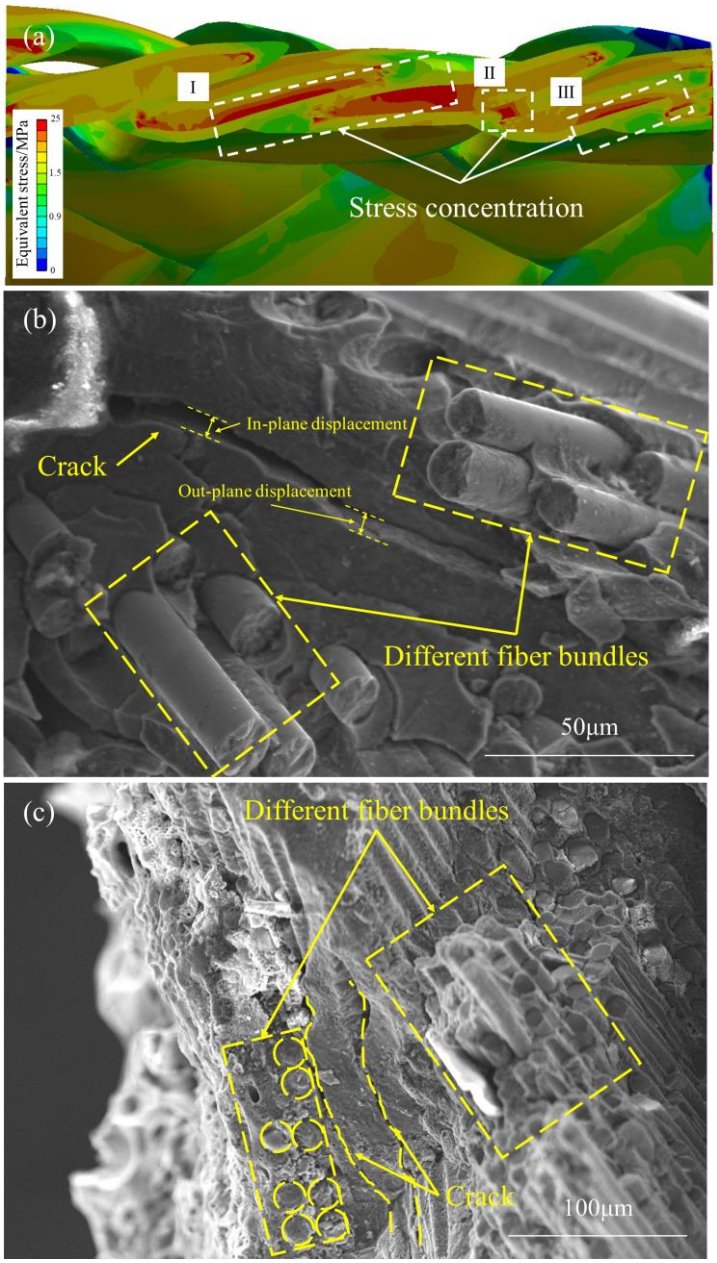

Fig. 10 (a) The predicted internal stress distribution of the specimen due to heating from 20°C to 1000°C; (b) and (c) the fracture morphology of specimen after 250 and 1250 thermal shock cycles, respectively

The fracture surface of a specimen tested after 1250 thermal shock cycles is shown in the Fig. 10(c). The dotted boxes in the Fig. 10(c) indicate the location of the fiber bundles, and two initiated cracks can be found between the fiber bundles, one of which is close to the edge of the fiber bundle. The crack position is similar to that of area I and

III in the Fig. 10(a). The fibers in the outer fiber bundle show little pull-out, which is attributed to oxidation of the fiber-matrix interface. Oxidation increases the interface strength, which makes fiber pull out difficult [36].

The progressive change in fracture behavior is illustrated by comparison of samples tested after 0, 500, and 1000 thermal shock cycles (Fig. 11). The regions of outer fiber bundles are marked by the two thick yellow dotted lines. Oxidized regions where almost no pullout of fibers is observed are labelled as "embrittled". Conversely, the non-oxidized regions, where fiber pullout is observed, are labelled as "non-embrittled". Embrittled regions are not observed on the fracture surface of the specimen with no thermal shock cycles (Fig. 11(a)). For the specimen tested after 500 thermal shock cycles, the outer fiber bundles show some embrittled behavior due to oxidation (Fig. 11(b)), and the specimen tested after 1000 thermal shock cycles shows an embrittled region that had spread over the whole outer fiber bundles (Fig. 11(c)). With the increase of thermal shock cycles, the embrittled region extends more deeply from the outer surface. It is deduced that microcracks, due to thermal tensile stresses, allow penetration of the oxidizing environment to the fiber/matrix interfaces, and the progressive oxidation and embrittlement of the composite microstructure increases in depth with increasing number of thermal cycles.

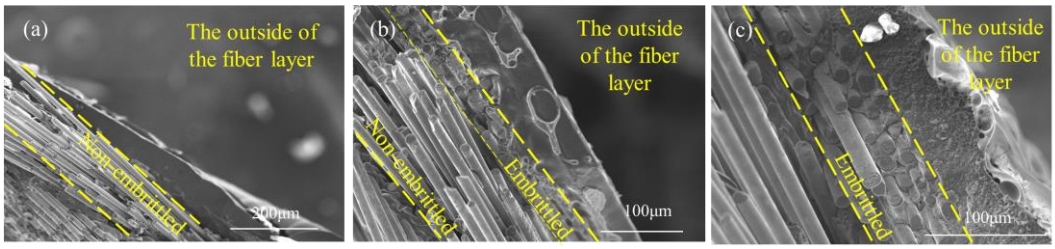

Fig. 11 The fracture morphology of the specimen: (a), (b) and (c) 0, 500 and 1000 thermal shock cycles

There is gradual reduction of the maximum load that the outer fiber layer can bear with increasing number of thermal cycles as the extent of oxidation embrittlement increases. Simultaneously, the fracture behavior of the specimen becomes more pseudoplastic, as shown in Fig. 7. Cheng et al. [37] examined the pseudoplastic fracture behaviors of CMCs, and found that this occurs because the fibers tend to fracture gradually in a relatively small groups with a structural unit of fracture that is mainly the

fiber clusters. It may be inferred that with the increase of thermal shock cycles, matrix cracking weakens the connections between the fiber bundles. This contributes to more aggregation of fracture during the C-ring test, which leads to the pseudoplastic fracture behavior. The stable or 'graceful' failure with pseudoplastic fracture also arises from the reduction in stored elastic strain energy in the specimen that accompanies the reduction in maximum load with progressive oxidation from increasing numbers of thermal cycles.

4. Conclusion

A thermal shock test platform based on quartz lamp irradiation heating, which can simulate fast temperature cycling environments, was used to study the thermal shock resistance of SiC/SiC composite braided tubes. The circumferential tensile strength after thermal shock cycling was measured using diametral testing of C-ring specimens. The following conclusions were drawn.

(1) An oxidized region of the fiber bundles, which fails with negligible fiber pullout, spreads from the outer surface with increasing number of thermal shock cycle. Microcracking of the SiC matrix, due to thermal tensile stresses, provides a pathway for the oxidizing environment to the fiber/matrix interfaces in the fiber bundles. This leads to a gradual reduction of the maximum tensile stress that the outer fiber bundles can bear. The outer fiber bundles are completely oxidized after 1000 thermal shock cycles.

(2) With the increase of thermal shock cycles, the failure mode of the SiC/SiC braided composite C-ring specimen changes from brittle to pseudoplastic fracture. This is deduced to be due to the accumulation of microcracking damage in the outer fiber bundles.

(3) The residual circumferential tensile strength of the SiC/SiC braided composite tubes presents an obvious declining trend with the number of thermal shock cycles increase. A linear formula describes a degradation relationship that is suitable for engineering applications.

Acknowledgment

This work is supported by National Science and Technology Major Project (J2019-

IV-0003-0070), the National Natural Science Foundation of China (12102320) and China Postdoctoral Science Foundation (2021M692571).

Appendix

According to curved beam theory [38], the circumferential stress at position y is

$$\sigma_\theta = -\frac{F}{A} + \frac{M}{AR} - \frac{M}{J_z}\frac{y}{1-\frac{y}{R}} \tag{3}$$

where R is radius (at the mid-thickness of the tube wall), F is the force, y is the coordinate in the Y direction (y=0 at the mid-thickness of the tube wall), as illustrated in Fig. 12, A is the cross-sectional area, and M is the bending moment.

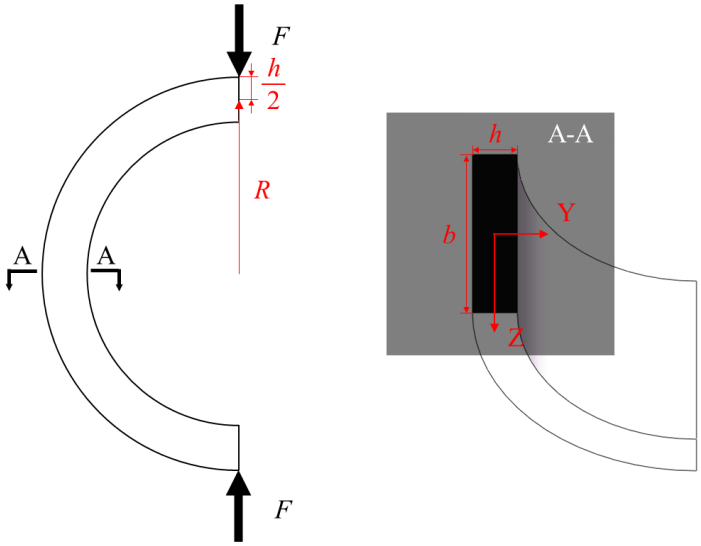

Fig. 12 The defined geometry parameters of C-shaped specimen and cross-section A-A.

The expression of J_Z is as follows:

$$J_z = \int_A \frac{y^2 dA}{(1-\frac{y}{R})} \tag{4}$$

For the C-shaped specimen, failure tends to propagate from the symmetrical position of the specimen (i.e., A-A plane). On the A-A plane, the cross-sectional area and the bending moment are

$$A = bh \tag{5}$$

$$M = FR \tag{6}$$

For rectangular sections,

$$J_z = \int_A \frac{y^2 dA}{1-\frac{y}{R}} = \int_{-\frac{h}{2}}^{\frac{h}{2}} (y^2 + \frac{y^4}{R^2} + \frac{y^6}{R^4} + ...) b dy$$
$$= \frac{bh^3}{12}(1 + \frac{3h^2}{20R^2} + \frac{3h^4}{112R^4} + ...) \quad (7)$$

It can be found that

$$J_Z = \begin{cases} 1.177 I_z, & R = h \\ 1.039 I_z, & R = 2h \\ 1.017 I_z, & R = 3h \\ 1.009 I_z, & R = 4h \end{cases} \quad (8)$$

Therefore, in order to simplify the calculation, it is assumed that $J_Z \approx I_Z$, R=4.5 mm and h=1 mm. Then, circumferential stress at the peak load can be calculated as

$$\sigma_\theta = -\frac{12FR}{bh^3} \frac{y}{1-\frac{y}{R}} \quad (9)$$

As can be seen from Eq. (9), when $y=h/2$, σ_θ has the maximum value $\sigma_{\theta\max}$.

$$\sigma_{\theta\max} = \frac{6FR}{bh^2(1+\frac{h}{2R})} \quad (10)$$

Declarations

Conflict of Interest The authors declare that there is no conflict of interest regarding the publication of this article.

References

[1] Jin XC, Marrow TJ, Wang JR, et al (2022) Crack propagation in fine grained graphites under mode I and mixed-mode loading, as observed in situ by microtomography. Carbon 193(30):356-367. https://doi.org/10.1016/j.carbon.2022.03.051

[2] Chen G, Peng YB, Zheng G, et al (2016) Polysynthetic twinned TiAl single crystals for high-temperature applications. Nat Mater 15: 876. https://doi.org/10.1038/nmat4677

[3] Perepezko JH (2009) The Hotter the Engine, the Better. Science 326(5956): 1068–

1069. https://doi.org/10.1126/science.1179327

[4] Azevedo CRF (2011) Selection of fuel cladding material for nuclear fission reactors. Eng Fail Anal 18(8):1943-1962. https://doi.org/10.1016/j.engfailanal.2011.06.010

[5] Padture NP (2016) Advanced structural ceramics in aerospace propulsion. Nat Mater 15(8):804. https://doi.org/10.1038/nmat4687

[6] Wang L, Wu JY, Chen CY, et al (2017) Progressive failure analysis of 2D woven composites at the meso-micro scale. Compos Struct 178: 395-405. http://dx.doi.org/10.1016/j.compstruct.2017.07.023

[7] Liu CQ, Chen Y, Shi DQ, et al (2021) In Situ Investigation of Failure in 3D Braided SiCf/SiC Composites under Flexural Loading. Compos Struct 270(15):114067. https://doi.org/10.1016/j.compstruct.2021.114067

[8] Azevedo C (2011) Selection of fuel cladding material for nuclear fission reactors. Eng Fail Anal 18(8):1943-1962. https://doi.org/10.1016/j.engfailanal.2011.06.010

[9] Wang L, Zhao B, Wu JY, et al (2018) Experimental and numerical investigation on mechanical behaviors of woven fabric composites under off-axial loading. Int J Mech Sci 141: 157-167. https://doi.org/10.1016/j.ijmecsci.2018.03.030

[10] Zoli L, Vinci A, Galizia P. et al (2018) On the thermal shock resistance and mechanical properties of novel unidirectional UHTCMCs for extreme environments. Sci Rep 8(1): 9148. https://doi.org/10.1038/s41598-018-27328-x

[11] Yang ZM, Huang Y, Hui L (2019) Evolution and characterization of cyclic thermal shock-induced thermomechanical damage in oxide/oxide ceramics matrix composites. Int J Fatigue 120(2019): 150–161. https://doi.org/10.1016/j.ijfatigue.2018.11.006

[12] Tong YG, Zhu WT, Bai SX, et al (2018) Thermal shock resistance of continuous carbon fiber reinforced ZrC based ultra-high temperature ceramic composites prepared via Zr-Si alloyed melt infiltration. Mat Sci Eng A 735(2018): 166-172. https://doi.org/10.1016/j.msea.2018.08.036

[13] Yang ZM, Liu H (2020) Effects of thermal aging on the cyclic thermal shock behavior of oxide/oxide ceramic matrix composites. Mat Sci Eng A 769(2020):

138494. https://doi.org/10.1016/j.msea.2019.138494

[14] Wang HY, Singh RN, Lowden RA (1996) Thermal shock behavior of two-dimensional woven fiber-reinforced ceramic composites. J Am Ceram Soc 79(7):1783–92. https://doi.org/10.1111/j.1151-2916.1996.tb07996.x

[15] Bayerl T, Duhovic M, Mitschang P, et al (2014) The heating of polymer composites by electromagnetic induction – A review. Compos Part Aappl S 57:27-40. https://doi.org/10.1016/j.compositesa.2013.10.024

[16] Wang WH, Li J (2011) A Method for Calculating Heat Energy and Braking Moment of Automobile Electromagnetic Retarder with Skin Effect. In: Advances in Computer Science, Intelligent System and Environment, Advances in Intelligent and Soft Computing. Heidelberg, Berlin, pp 289–295. https://doi.org/10.1007/978-3-642-23753-9_46

[17] Bereza J, Sadowski J, Teodorczyk T (2007) Direct resistance heating of steel elements. Prz Elektrotechniczn 83(3):88-89

[18] Zhang Z, Zhang JS, Yue MK, et al (2021) High-temperature thermal expansion behaviour of C/SiC studied using an in-situ optical visualisation method and numerical simulations in a quartz lamp array heating environment. Ceram Int 47(9):12547-12556. https://doi.org/10.1016/j.ceramint.2021.01.112

[19] Cabet C, Michaux A, Fazio C, et al (2013) The new EC FP7 MatISSE project: materials' innovations for a safe and sustainable nuclear in Europe. In: SMINS-3, Structural Materials for Innovative Nuclear Systems (SMINS-3) - Workshop Proceedings, Idaho National Laboratory, Idaho Falls, United States pp 7-10

[20] Braun J, Sauder C, Lamon J, Balbaud-Célérier F (2019) Influence of an original manufacturing process on the properties and microstructure of SiC/SiC tubular composites. Compos Part A-Appl S 123:170–179. https://doi.org/10.1016/j.compositesa.2019.04.031

[21] Zhao SX (2018) 3D multi-scale characterization and modelling of damage in ceramic matrix composites. University of Oxford, Trinity College, UK (PhD)

[22] Ayranci C, Carey J (2008) 2D braided composites: A review for stiffness critical applications. Compos Struct 85(1):43-58.

https://doi.org/10.1016/j.compstruct.2007.10.004

[23] Wang R, Zhang L, Hu D, et al (2017) A novel approach to impose periodic boundary condition on braided composite RVE model based on RPIM. Compos Struct 163:77-88. https://doi.org/10.1016/j.compstruct.2016.12.032

[24] Dong J, Huo N (2016) A two-scale method for predicting the mechanical properties of 3D braided composites with internal defects. Compos Struct 152:1-10. https://doi.org/10.1016/j.compstruct.2016.05.025

[25] Wang RQ, Zhang L, et al (2017) Evaluation of three unit cell models in predicting the mechanical behaviour of 3D four-directional braided composites. J Compos Mater 51(27):3757-3767. https://doi.org/10.1177/0021998317692657

[26] Shen X, Liu X, Dong S, et al (2018) RVE Model with Shape and Position Defects for Predicting Mechanical Properties of 3D Braided CVI-SiCf/SiC Composites. Compos Struct 195:325-334. https://doi.org/10.1016/j.compstruct.2018.04.074

[27] Wen Z, Zhang XH, Yue X, et al (2021) FEM analysis of the stress response and failure mechanism of SiC-coated Cf/SiC composites during thermal shock. Ceram Int 47(15): 21996-22005. https://doi.org/10.1016/j.ceramint.2021.04.218

[28] Sauder C, Michaux A, Loupias G, et al (2013) Assessment of SiC/SiC cladding for LWRs. In: LWR Fuel Performance Meeting Top Fuel 2013. Charlotte, NC, pp 951–956

[29] Arregui-Mena JD, Koyanagi T, Cakmak E, et al (2022) Qualitative and quantitative analysis of neutron irradiation effects in SiC/SiC composites using X-ray computed tomography. Compos Part B-eng 238: 109896. https://doi.org/10.1016/j.compositesb.2022.109896

[30] Ferber MK, Tennery VJ, Waters SB, et al (1986) Fracture strength characterization of tubular ceramic materials using a simple c-ring geometry. J Mater Sci 21(8):2628-2632. https://doi.org/10.1007/BF00551464

[31] Wolfenden A, Shelleman DL, Jadaan OM, et al (1991) Prediction of the Strength of Ceramic Tubular Components: Part II—Experimental Verification. J Test Eval 19(3):192-200. https://doi.org/10.1520/JTE12556J

[32] ASTM C1323−10 (2010) Standard Test Method for Ultimate Strength of

Advanced Ceramics with Diametrally Compressed C-Ring Specimens at Ambient Temperature, ASTM International, West Conshohocken, PA. https://doi.org/10.1520/C1323-22

[33] Saucedo-Mora L, Lowe T, Zhao S, et al (2016) In situ observation of mechanical damage within a SiC-SiC ceramic matrix composite. J Nucl Mater 481:13–23. https://doi.org/10.1016/j.jnucmat.2016.09.007

[34] Jacobsen GM, Stone JD, Khalifa HE, et al (2014) Investigation of the C-ring test for measuring hoop tensile strength of nuclear grade ceramic composites. J Nucl Mater 452(1-3):125-132. https://doi.org/10.1016/j.jnucmat.2014.05.002

[35] Alabdullah M, Ghoniem NM (2020) A thermodynamics-based damage model for the non-linear mechanical behavior of SiC/SiC ceramic matrix composites in irradiation and thermal environments. Int J Damage Mech 29(10):1569-1599. https://doi.org/10.1177/1056789520941574

[36] Panakarajupally RP, Kannan M, Morscher GN (2021) Tension-tension fatigue behavior of a melt-infiltrated SiC/SiC ceramic matrix composites in a combustion environment. J Eur Ceram Soc 41(5):3094-3107. https://doi.org/10.1016/j.jeurceramsoc.2020.10.007

[37] Cheng LF, Zhang LT, Mei H (2018) Strengthening, toughening and application basis of ceramic matrix composites. Chemical Industry Press, Beijing (in Chinese)

[38] Liu HW (1985) Advanced material mechanics. Higher Education Press, Beijing (in Chinese)